Quantum Electronics **47** (6) 495–502 (2017)

INTERACTION OF LASER RADIATION WITH MATTER. LASER PLASMA https://doi.org/10.1070/QEL16292

Interaction of high-power laser radiation with low-density polymer aerogels*

Ch. Kaur, Sh. Chaurasia, N.G. Borisenko, A.S. Orekhov, P. Leshma, V.G. Pimenov, G.V. Sklizkov, A.A. Akunets, M.N. Deo

Abstract. **The interaction of high-power subnanosecond laser pulses with low-density targets of cellulose triacetate polymer is considered. An Nd-glass laser setup provides a focal spot intensity of over 10^{14} W cm^{-2}. An investigation is made of absorption of laser radiation, laser-to-X-ray energy conversion, spectra of ions emitted from the plasma, transmission of laser radiation through the target and plasma, as well as volume heating of the target material. It is experimentally determined that the laser energy conversion efficiency to X-rays with photon energies of a few kiloelectronvolts decreases with increasing target material density. With the use of targets of density 10 mg cm^{-3} this efficiency is two times lower in comparison to 2 mg cm^{-3} density targets. The duration and amplitude of laser pulses transmitted through the target decreases with increasing column target density (the product of target material density and its thickness). The spectra of ions emitted from low-density target plasmas are recorded using ion collectors positioned at different angles relative to the direction of laser beam propagation as well as a high-resolution Thomson mass spectrometer. The ion flux and ion energies are found to increase with increasing target material density. The peak of the ion energy spectrum is shifted towards higher energies with increasing laser radiation intensity.**

Keywords: *laser-produced plasma, nanostructures, ion spectroscopy, low-density aerogel, volume absorption, subcritical-density targets, X-ray radiation yield.*

1. Introduction

Laser-produced plasma X-ray sources show promise for applications in many research areas such as indirect inertial confinement fusion [1], X-ray microscopy [2], X-ray lithography [3], X-ray radiography [4], diffraction measurements of materials under extreme conditions [5], transparency measurements [6], etc. However, laser-to-X-ray energy conversion efficiency of solid targets is usually too low owing to the reflection of most of light energy and reduced laser absorption energy for supercritical plasma densities. The fraction of laser energy absorbed in the target plasma can be increased in different ways. It is possible to use a laser prepulse to produce a plasma corona prior to the arrival of the main pulse, so that the latter would interact with this low density preplasma as a result path of absorption in the rarefied subcritical-density plasma would therefore become longer [7]. Another way involves use of mixed-composition targets with different ion charge states Z to improve the conversion efficiency by increasing the Rosseland mean opacity coefficient in the mixture of ion charge states [8]. Lastly, the X-ray yield may be improved by displacing the target relative to the best-focus position, which is termed the plasma volume effect [9]. In recent years, to achieve a higher X-ray yield, many experiments and theoretical simulations have been carried out on gas targets [10] and with structured targets [11], for instance, targets covered with nanoparticles or nanowires [12]. With a view to a longer path of absorption and volume absorption, foam* was developed of an aerogel structure in the form of a three-dimensional spatial network [13]. Targets with low-density three-dimensional networks make up a preferred class of materials, which offer certain advantages like the smoothing of the laser radiation profile [14], shock wave enhancement [15], etc. Foams with a density gradient have been employed for obtaining an inclined density profile for isentropic compression [16] and as a CH ablator in direct inertial confinement fusion [17].

Many authors have noted that foam targets provide a several times higher absorption than conventional solid targets and that these low-density targets are higher-efficiency emitters of X-ray radiation than solid full-density targets [18]. Considerable research interest is beeing shown in the interaction of high-power laser radiation with foam targets of a broad density range: from 1 mg cm^{-3} to hundreds of mg cm^{-3}, i.e. from subcritical densities to supercritical ones [19]. Low-density foam targets of different materials, which may be referred to as stochastically volume-structured targets, are capable of providing absorption of up to 90% of the energy of laser radiation incident on the target.

Foam targets are also used in the modelling of astrophysical effects in laboratory conditions [20]. For instance, these materials were employed in the modelling of the interaction of circumstellar matter with an exploding stellar shell as well

*Presented at the ECLIM 2016 conference (Moscow, 18–23 September 2016).

Ch. Kaur, Sh. Chaurasia, P. Leshma, M.N. Deo High-Pressure & Synchrotron Radiation Physics Division, Bhabha Atomic Research Centre, Mumbai 400085, India;
N.G. Borisenko, A.S. Orekhov, G.V. Sklizkov, A.A. Akunets P.N. Lebedev Physical Institute, Russian Academy of Sciences, Leninsky prosp. 53, 119991 Moscow, Russia; e-mail: ngbor@sci.lebedev.ru;
V.G. Pimenov N.D. Zelinsky Institute of Organic Chemistry, Russian Academy of Sciences, Leninsky prosp. 47, 119991 Moscow, Russia

Received 26 January 2017
Kvantovaya Elektronika **47** (6) 495–502 (2017)
Translated by E.N. Ragozin

*The slang term 'foam' is practically ineradicable from the literature and is used in our paper merely to honour the tradition.

as of the formation of supernovae remnants [21, 22]. Numerous attempts have been made to explain the enhanced X-ray radiation yield properties of foams. For instance, in the numerical simulations of a gold foam [23] it was found that the target heating was determined by the supersonic ionisation wave, unlike the heating of a continuous target. There are many experimental and theoretical data describing the emission of X-ray radiation from low-density foams. However, we have not found any papers concerned with a detailed analysis of the characteristics of the ions emitted by such targets. Our work is dedicated to precisely studying the hard X-ray emission along with the spectroscopic measurement of the ion flux from low-density target plasmas.

2. Experimental setup

Our experiment was carried out using an Nd-glass laser setup delivering a 500-ps long pulse with an energy of up to 30 J. In the experiments reported here the output pulse energy amounted to 10 J. An *f*/5 lens focused the laser pulse to a focal spot 100 μm in diameter, which corresponded to a peak intensity of 2.5×10^{14} W cm^{-2} at the target surface. The experimental setup is schematically shown in Fig. 1. To observe the plasma evolution (the emitted ions), four Faraday ion collectors were positioned at angles $\theta = 22.5°$, 45°, 63°, and 67.5° to the target surface normal, which coincided with the optical axis of the laser beam.

Ion collectors were Faraday cups with a flat collector and a grid for separating ions and electrons. The constant field existing between the grounded grid and the negatively biased collector serves to separate charged particles and removes the problems arising from the emission of secondary electrons. The grounded grid also rejects the primary electrons from the measured ion flux. Owing to their large area, Faraday detectors may be positioned far from the target for higher time-of-flight resolution.

Ion collectors record the integral ion flux for all ion charge states and energies emitted by the target in the course of interaction with the laser pulse. To distinguish the ions by their energy and charge state, use was made of a Thomson mass spectrometer with parallel electric and magnetic fields both perpendicular to the direction of ion flux motion. The ions that find their way to the spectrometer are deflected by the Lorentz force $\boldsymbol{F} = q(\boldsymbol{E} + \boldsymbol{v} \times \boldsymbol{B})$ in the direction parallel to the electric field $\boldsymbol{E}$ and perpendicular to the magnetic field $\boldsymbol{B}$ ($\boldsymbol{v}$ is the ion velocity, $q = Ze$ is the ion charge, and e is the electron charge). The ions of higher charge and lower kinetic energy will experience a larger deflection in this spectrometer.

The combined action of the electric and magnetic fields gives rise to parabolic traces on the detector screen. The equation describing their shape may be written in the form:

$$y = \left(\frac{\beta}{a^2}\frac{m}{Z}\frac{1}{e}\frac{E}{B^2}\right)x^2, \tag{1}$$

where α and β are the structure parameters [24].

Therefore, for fixed electric and magnetic fields, the ions with different mass/charge ratios (m/q) produce different parabolic traces on the detector. For a comprehensive description of the Thomson mass spectrometer and an analysis of the data obtained with its use, the reader is referred to Ref. [24].

The hard X-ray radiation flux was recorded by silicon photodiodes covered with different filters for studying different ranges of the X-ray spectrum: a 20-μm thick Al foil for extracting a range of 4–16 keV or a 5-μm thick Ni foil with a 5–8.3 keV transmission band. To measure the spatial and temporal shapes of the laser pulse transmitted through the low-density polymer target, a beam splitter was placed in the

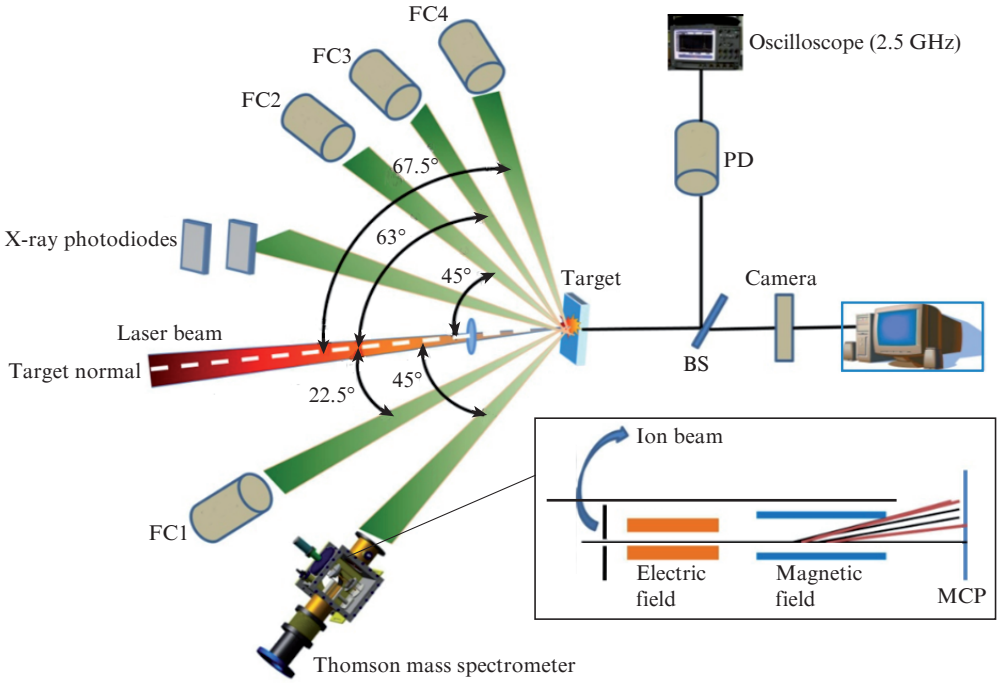

Figure 1. Schematic of the experimental setup: (FC1, FC2, FC3, and FC4) Faraday ion collectors; (PD) fast photodiode for measuring the temporal parameters of transmitted pulses; (BS) beam splitter; (MCP) microchannel plate; the laser beam is normally incident on the target; the inset shows the interior arrangement of the Thomson mass spectrometer.

path of the transmitted beam. In this case, one part of the beam was directed to a fast photodiode and the other part to a beam profile meter. An Alphalas photodiode with a rise time of 40 ps was connected to an Agilent Technologies oscilloscope with a transmission band of 2.5 GHz.

2.1. Targets

We employed almost visually transparent, plane-parallel samples of cellulose triacetate (CTA) $C_{12}H_{16}O_8$ with a highly regular structure in the form of a three-dimensional network – plymer aerogels (Fig. 2). All samples exhibited a high repeatability and had an invariable aerogel structure, which was laborious in fabrication and measurement [25]. The absence of closed pores and the stably repetitive structure of three-dimensional spatial network type of the low-density targets in use permit investigating the properties of the plasma produced under irradiation of these targets using different diagnostic techniques on the same setup at any time for a long period of time. These properties also enable comparing the resultant data with the experimental data obtained on other facilities [13, 19, 25]. Laboratory techniques of synthesising such targets were considered, for instance, in Ref. [26]. We emphasise that their mechanical properties are much different from the properties of silica aerogels.

In Fig. 2b one can see a small piece of the aerogel detached and elevated over the holder, which provides an idea about the transparency, uniformity, and fragility of the resultant nanostructured microobjects. Even a single touch makes the sample unsuitable for laser experiments by irretrievably damaging the structure of the solid polymer substance, which has the density of a gas.

3. Results and their discussion

3.1. Measurements of the transmittance for laser radiation

The temporal shape of the pulse transmitted through the low-density aerogel target was measured with a fast photodiode, which viewed the rear side of the target. To reject the intrinsic plasma radiation, a filter with a 10-nm transmission band centred at a laser wavelength of ~1064 nm was placed in front of the photodiode. Thus, harmonic generation and other nonlinear processes of laser radiation conversion in the target are not investigated in the present work. The laser pulse shape was measured at various attenuations in order not to overexpose the photodiode in the absence of a target in the chamber, whereas the photodiode calibration remained invariable for aerogel targets of different density and thickness. We found that the duration of the pulses transmitted through the targets was shorter for targets with a higher column density (the product of density ρ and thickness h). Specifically, for the target with a column density of about 600–900 mg cm^{-2} the FWHM pulse duration was equal to 360 ps for an initial pulse duration of 680 ps. When the column density was increased up to 2000 mg cm^{-2} (a 1-mm thick target with a density of 2 mg cm^{-3}), the pulse duration shortened further to 176 ps.

From Fig. 3 it follows that the target transmittance to the laser radiation depends mainly on the target column density and is independent of the density of the target material. Along with this, no difference in the leading edge of the pulse was observed for targets of different initial density. In this case, the trailing edge of the pulses was appreciably shortened due to absorption

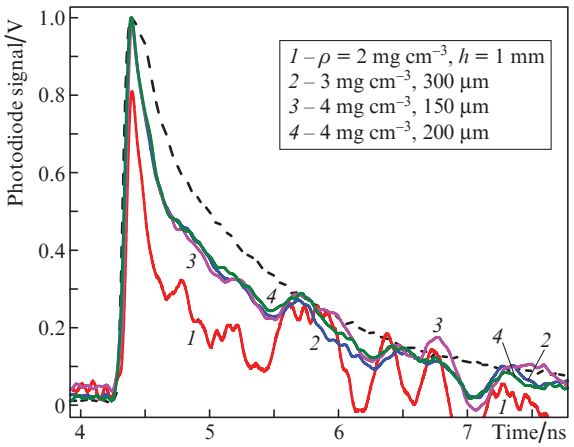

Figure 3. (Colour online) Temporal profiles of the initial pulse (the dashed curve) and the pulses transmitted through low-density CTA targets of different density and thickness (solid curves).

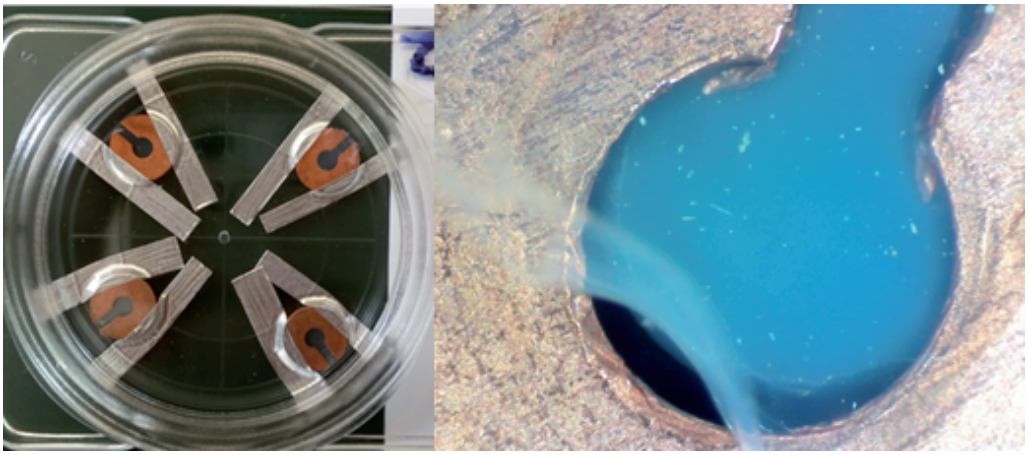

a b

Figure 2. (Colour online) CTA targets with a density of 4 mg cm^{-3}: (a) hermetic Millipore box with four targets on metallised mounts prepared for transportation to the laser setup and (b) a microphotograph of a CTA plastic aerogel sample (blue) inside a ring holder.

in the target. We attribute this behaviour to the short pulse rise time which is inherent in SBS compressed laser pulses as in our case. This fast rise time of the laser pulse is shorter than the time required for the whole plasma to reach the critical density and hence results in a reduced absorption of the leading edge and increased absorption at the trailing edge of the laser pulse when the plasma reaches a critical density, thereby modifying the transmitted laser pulse profile.

3.2. Investigation of X-ray radiation with photon energies of several kiloelectronvolts

The X-ray emission from aerogel targets was studied with the variation of laser radiation intensity at the surface of a target of fixed density or in relation to the target density for a laser pulse energy $W_L = 6.18$ J. Figure 4a shows the dependences of the X-ray yield Y_X on the energy W_L for spectral ranges of 4–16 keV and 5–8.3 keV. The observed dependences are well approximated by a power function $Y_X = W_L^{\gamma}$, where the exponent γ is equal with an accuracy of 10% to 2.3 and 1.8 for the ranges 4–16 keV and 5–8.3 keV, respectively. Figures 4b and 4c show the variation of the X-ray yield for the specified spectral ranges in relation to the target density*. For both spectral ranges the X-ray yield is 1.4–1.5 times higher for a foam target with a subcritical density of 2 mg cm^{-3} in comparison with the target with a supercritical density of 10 mg cm^{-3}. There are two main reasons for the higher X-ray yield of lower-density targets: the existence of supersonic ionisation and thermal waves resulting in volume target heating as well as the absence of heating energy loss for the hydrodynamic ion motion. In this case, the absorption of laser radiation in aerogel materials depends on the thickness/diameter of the fibres of their constituent material and on the spacing between the fibres (i.e. on the pore dimensions).

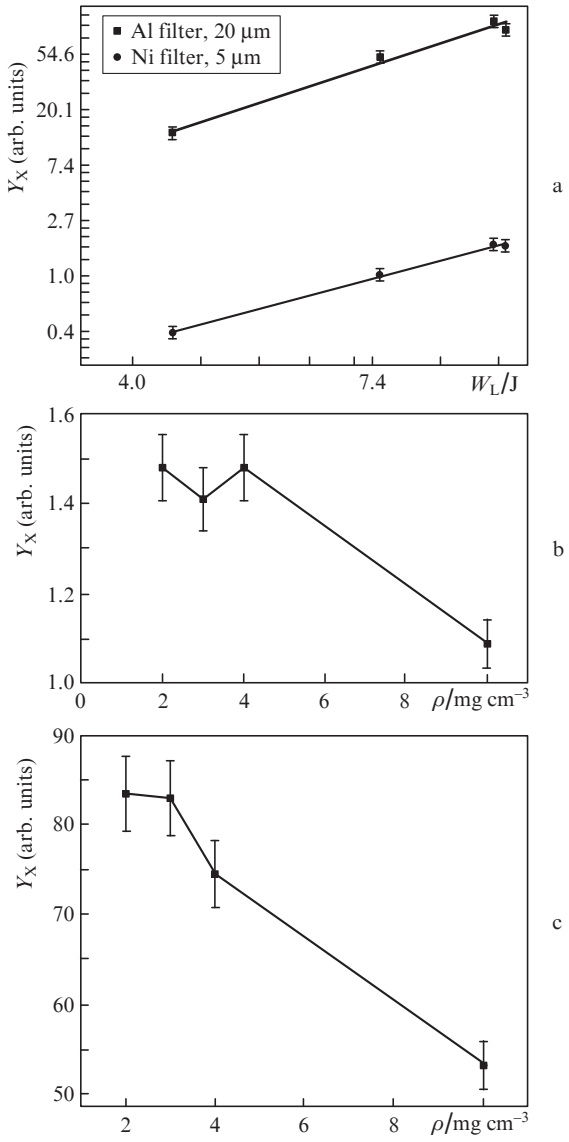

Figure 4. Dependences of the hard X-ray yield Y_X on the energy of a laser pulse W_L for a CTA target of density 4 mg cm^{-3} (a) and on the target density ρ for a laser radiation energy of 6.18 J in the ranges 5–8.3 (b) and 4–16 keV (c).

When the beam cross section spans the expanding solid elements of the spatial target network, the absorption length along the beam axis may be treated as the length of geometrical transparency (this is true until the density everywhere reaches the critical density or exceeds it due to the expansion of the individual elements of the network). In accordance with Ref. [27], this length is described by the expression

$$L_t = \frac{9.2\times10^{-8}}{Z}\left(\frac{A}{Z}\right)^2 \frac{T^{3/2}}{\lambda^2\rho^2}, \qquad (2)$$

where A is the atomic number; λ is the wavelength of laser radiation in μm; T is the electron temperature in keV; and ρ is expressed in g cm^{-3}.

One can see from formula (2) that the absorption length for laser radiation is inversely proportional to the squared foam (plasma) density. Specifically, for a subcritical density target the transparency length and therefore the X-ray emitting plasma volume turn out to be larger than for supercritical density targets. The radiation absorbed in a low-density plasma acts like a strong explosion, and ionisation and thermal waves propagate at a supersonic velocity in all directions to produce a large (nearly spherical) volume radiating in the X-ray range. By contrast, in supercritical density targets (or domains) the geometrical transparency domain is by far smaller and hence a smaller volume is heated, resulting in a lower X-ray yield.

Another cause of the lower X-ray yield for supercritical density targets is the energy loss due to the hydrodynamic ion motion. In the case of subcritical plasma, the plasma heating is supersonic in which case no hydrodynamic motion in the form of shock wave takes place; hence, there is no loss of absorbed laser energy for the hydrodynamic motion of plasma. In the case of supercritical plasma, the heating is not supersonic resulting in production of a hydrodynamic shock wave and transfer of absorbed laser energy to the kinetic energy of the shock wave, thereby lowering the efficiency of laser energy conversion to X-ray energy. Numerical simulations performed with the use of a one-dimensional multigroup radiative-hydrodynamic code (RDMG) in Ref. [28] confirmed the supersonic heating and absence of shock waves in the subcritical plasma. In the supercritical plasma the situation is opposite.

*The critical density for a CTA target irradiated by the laser radiation with a wavelength of 1.06 μm amounts to ~3 mg cm^{-3}.

3.3. Spectroscopy of the ion flux from low-density targets

The emission of ions from the targets of different density was studied using a high-resolution Thomson mass spectrometer and ion collectors. Data analysis showed that the ion flux increases with increasing laser intensity for a fixed target material density. Figure 5a shows the ion fluxes recorded by four ion collectors as functions of the laser intensity for a target of density 4 mg cm^{-3}. The scaling factors for the signals from the ion collectors placed at angles θ = 22.5°, 45°, 63°, and 67.5° with the target normal were equal to 0.5, 1.04, 1.3, and 0.8, respectively. The ion fluxes and their thermal velocities rise with increase in target material density from 2 to 10 mg cm^{-3} (Figs 5b and 5c).

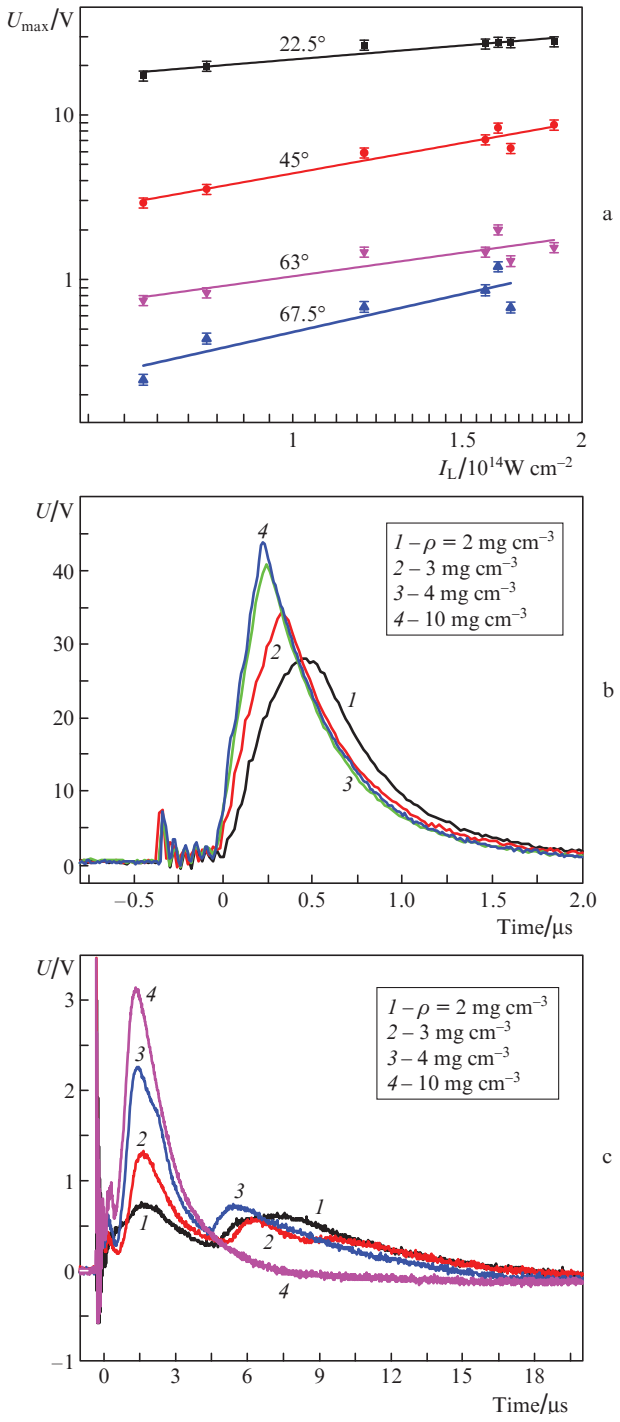

Figure 5. (Colour online) Dependences of the ion-collector signal amplitudes U_{max} on the laser intensity I_L at the surface of a CTA target with a density of 4 mg cm^{-3} (a) and time dependences of the ion signals U for collectors located at angles of 22.5° (b) and 67.5° (c) for CTA targets of different density and a laser energy of ~4.9 J.

One can also see in Fig. 5 that the signal from the ion collector placed at an angle of 67.5° with the target normal consists of two peaks for low-density targets. The spacing between the peaks becomes shorter with increasing target density (Fig. 5c). For a target density of 10 mg cm^{-3} these peaks merge into one. This behaviour may be due to the fact that the highest ion flux and ion velocities correspond to the direction along the normal to the surface, and their values decrease with icreasing distance from the normal. The two peaks in the curves obtained with the ion collector are primarily due to the low CTA target density and correspond to the clearly separated signals produced by fast and thermal ions under these conditions [29]. However, for a high target density the number of ions with different energies is large and therefore the two peaks merge. In principle, by processing the signals generated with high-density targets these peaks may be extracted.

Figure 6 depicts the ion flux and ion velocity angular distributions for the targets of different density for a fixed energy (4.9 J) of laser pulses. The angular ion flux distribution P peaks in the direction of the target normal and obeys the law $P(\theta) = P_0\cos^n\theta$, where P_0 is the ion flux along the normal. The exponent n was estimated with an accuracy of 10% at 4.1, 3.7, 3.3, and 3.0 for targets with densities of 2, 3, 4, and 10 mg cm^{-3}, respectively.

The angular ion velocity distribution shown in Fig. 6b is approximately isotropic for subcritical density targets, while the ion flux is lower in this case than for supercritical targets. This fact also bears out the explosion interpretation proposed above, which involves a supersonic thermal wave propagating in all directions, while the laser radiation is absorbed over the geometrical transparency depth. A similar observation was made in the course of previous investigations on CTA targets [19]: among the available shadowgraphs for targets of different density (from 2 to 50 mg cm^{-3}), isotropic plasma expansion takes place for subcritical density targets (i.e. for these targets the transverse plasma dimension, like its longitudinal dimension, is several times greater than the size of the focal spot of laser radiation on the target surface).

The Thomson mass spectrometer was employed for measuring the ion spectra of carbon and oxygen. Figure 7 depicts the images of spectra recorded for targets of different density. One can see in Figs 8a and 8b, which shows the ion spectra calculated from these images, that the high-energy ion flux increases with increasing target density. For instance, with an increase in target density the carbon C^{5+} and oxygen O^{6+} ion spectra broaden with retention of the total flux of these ions. We note that the same dependence is observed for the signals from the ion collectors (see Fig. 5).

The cause of low fluxes and low ion velocities for subcritical density ions may lie with the fact that the plasma is heated with a supersonic rate and uniformly, which results in the suppression of absorbed energy transfer to the hydrodynamic ion motion. For supercritical density targets the substance is heated with a subsonic rate, and the ions acquire energy for hydrodynamic motion, which affects their flux and energy spectrum.

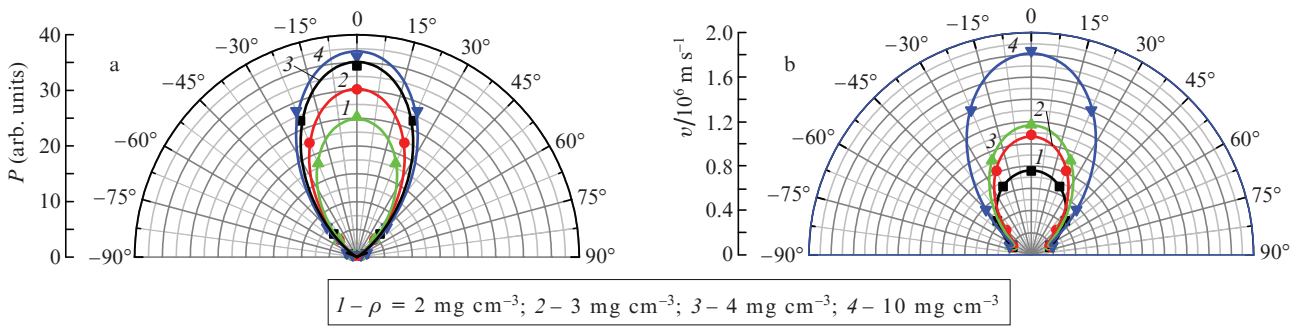

Figure 6. Calculated (curves) and experimental (points) angular distributions of the ion flux P (a) and the ion velocities v (b) for CTA targets of different density for a laser energy of ~4.9 J.

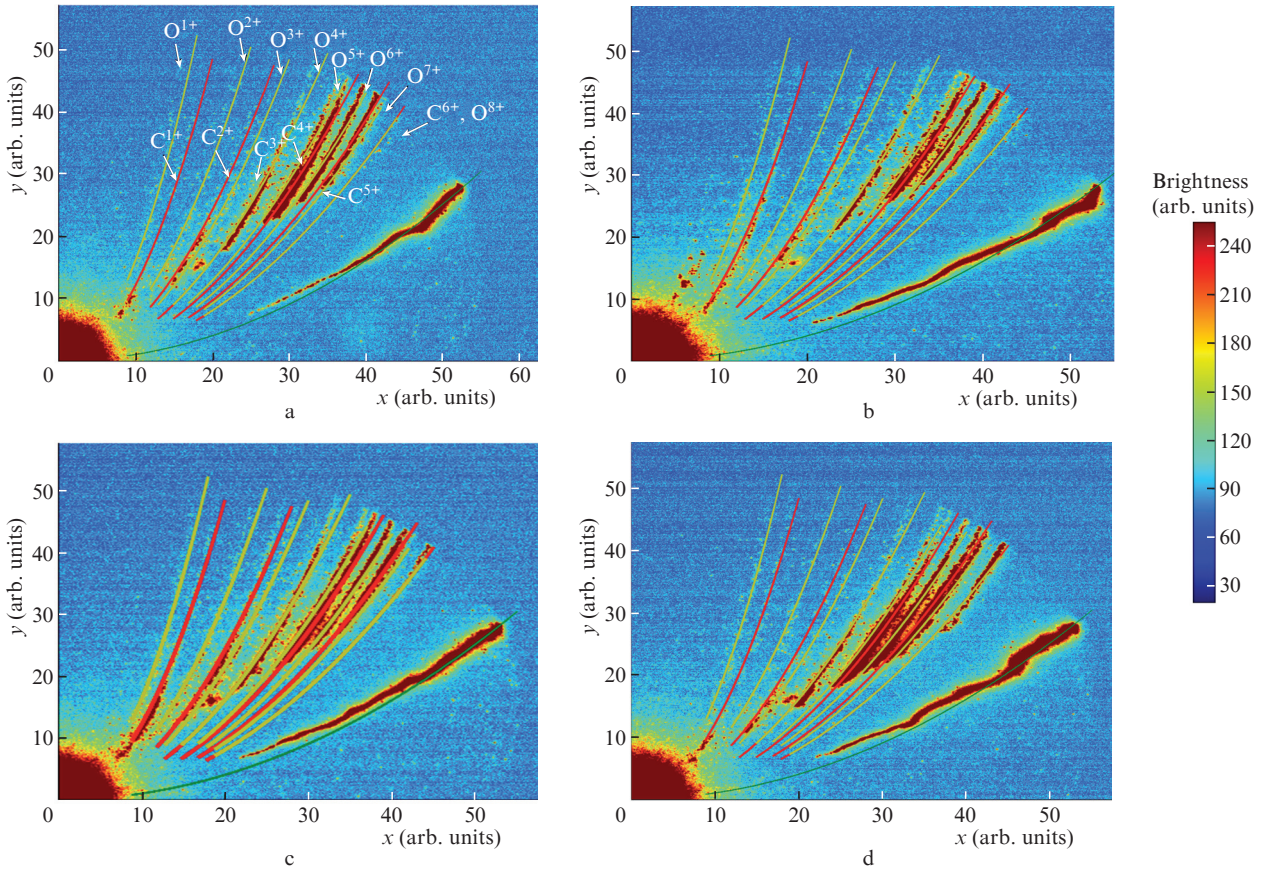

Figure 7. (Colour online) Images obtained with the Thomson mass spectrometer for CTA targets with a density of 2 (a), 3 (b), 4 (c), and 10 mg cm^{-3} (d) for a laser energy of ~4.9 J superimposed with the calculated curves for oxygen (yellow curves) and carbon (red curves) ions.

Figures 8c and 8d show the effect of laser energy on the C^{4+} and O^{5+} energy spectra for targets of density 4 mg cm^{-3}. With increasing laser pulse energy the ion fluxes rise and the peaks of ion spectra shift to higher energies.

4. Conclusions

This work describes the results of experiments on the interaction of laser pulses of moderate intensity (30 J, 500 ps) at a wavelength of 1064 nm with aerogel CTA targets with a density ranging from a subcritical density to three times the critical density. The characteristics were studied, including the transmitted laser radiation, the yield of X-ray radiation with photon energies of several kiloelectronvolts, and the emission of ions from the plasma. The effects of target density and laser radiation intensity on these characteristics were analysed. The duration and amplitude of transmitted laser pulses were shown to decrease with increasing column target density. Specifically, the pulse duration shortened from 680 ps (FWHM) to 360 ps after passage through the targets with a column density of about 600–900 mg cm^{-2} and to 176 ps for a target with a column density of about 2000 mg cm^{-2} (density ρ = 2 mg cm^{-3}, thickness h = 1000 μm). The pulsed laser irradiation of a subcritical density target was found to give rise to harder X-rays than the irradiation of a supercritical density

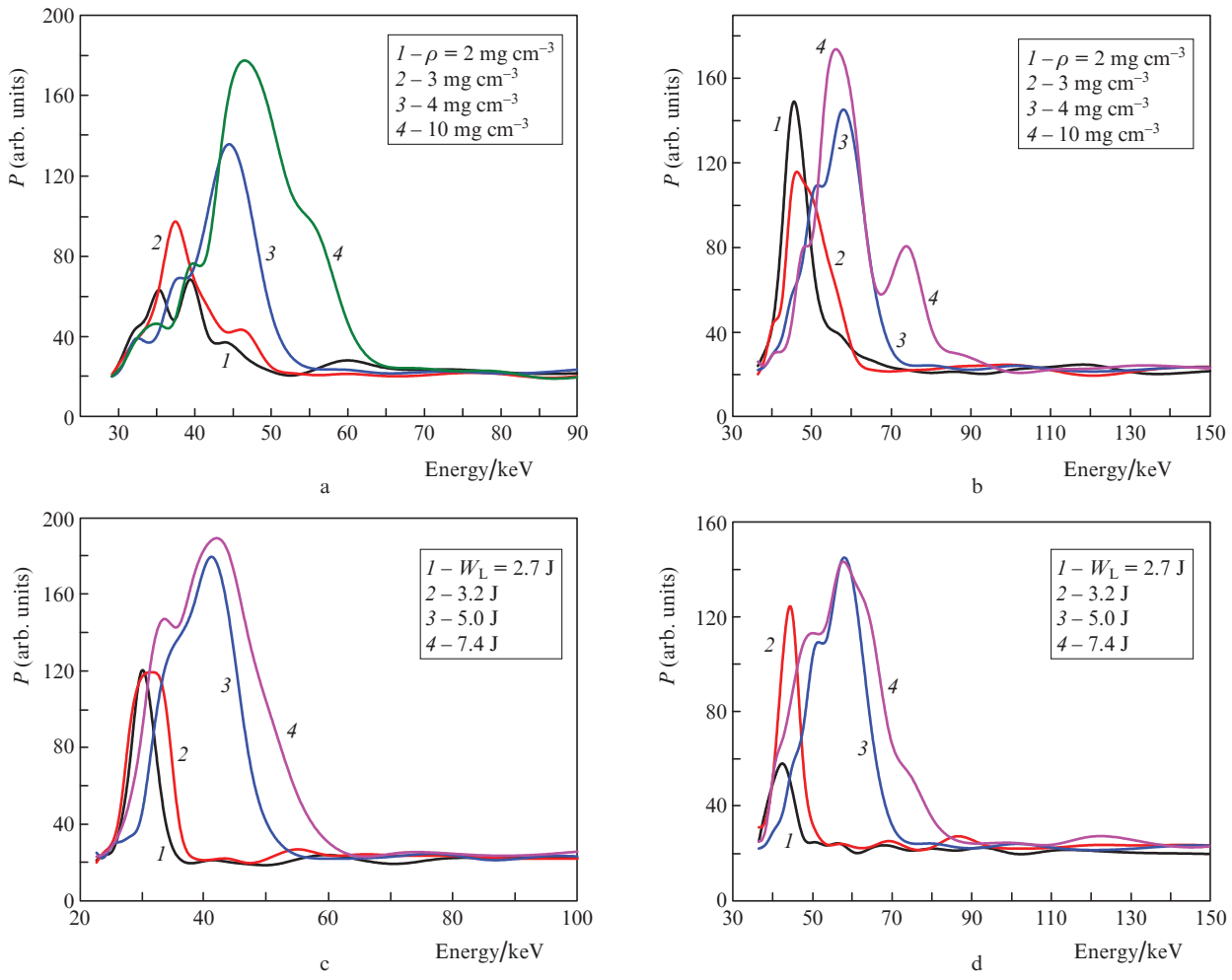

Figure 8. (Colour online) Energy spectra of C^{5+} (a) and O^{6+} ions for CTA targets of different density for a laser energy of ~4.9 J as well as of C^{4+} (c) and O^{5+} (d) ions for CTA targets of density 4 mg cm^{-3} for different laser energies W_L.

target. This may be due to the supersonic and volume heating of the subcritical density targets by a thermal wave as well as to the absence of significant energy loss for hydrodynamic ion motion. An analysis of the ion emission revealed an increase in ion flux and a shift of ion energy spectrum to higher energies in going to supercritical density targets.

Acknowledgements. The authors are thankful to S.M. Sharma and N.K. Sahoo (BARC) as well as to researchers of the Laboratory of Thermonuclear Targets of the P.N. Lebedev Physical Institute for their constant support. The authors express their appreciation to Sri C.G. Murali, Sri D.S. Munda, Ritesh Sable, and Krishna Bangre for the maintenance of the laser system and provision of data collection facilities during the experiments.

The Indian authors are thankful to the Department of Science and Technology (DST) for support and the possibility to carry out the experiments. The Russian authors acknowledge the support from the Russian Foundation for Basic Research (Grant No. 15-52-45116).

References

1. Marshall F.J., Oertel J.A. *Rev. Sci. Instrum.*, **68**, 735 (1997).
2. Förstera E., Gäbel K., Uschmanna I. *Laser Part. Beams*, **9**, 135 (1989).
3. Chaker M., Pepin H., Bareau V., Lafontaine B., Toubhans I., Fabbro R., Faral B. *J. Appl. Phys.*, **63** (3), 892 (1988).
4. Lewis C.L.S., McGlinchey J. *Opt. Commun.*, **53** (3), 179 (1985).
5. Miaja-Avila L., O'Neil G.C., Uhlig J., Cromer C.L., Dowell M.L., Jimenez R., Hoover A.S., Silverman K.L., Ullom J.N. *Structural Dynamics*, **2** (2), 024301 (2015).
6. Rossall A.K., Gartside L.M.R., Chaurasia S., Tripathi S., Munda D.S., Gupta N.K., Dhareshwar L.J., Gaffney J., Rose S.J., Tallents G.J. *J. Phys. B: At. Mol. Opt. Phys.*, **43** (15), 155403 (2010).
7. Andreev A.A., Limpouch J., Iskakov A.B., Nakano H. *Phys. Rev. E*, **65** (2), 026403 (2002).
8. Chaurasia S., Murali C.G., Munda D.S., Gupta N.K., Dhareshwar L.J. *J. Appl. Phys.*, **103**, 13307 (2008).
9. Chaurasia S., Tripathi S., Leshma P., Murali C.G., Pasley J. *Opt. Commun.*, **308**, 169 (2013).
10. Fiedorowicz H., Bartnik A., Jarocki R., Rakowski R., Szczurek M. *Appl. Phys. B*, **70**, 305 (2000).
11. Mahdieh M.H., Fazeli R., Tallents G.J. *J. Phys. B: At. Mol. Opt. Phys.*, **42** (12), 125602 (2009).
12. Rajeev P.P., Taneja P., Ayyub P., Sandhu A.S., Ravindra Kumar G. *Phys. Rev. Lett.*, **90** (11), 115002 (2003).
13. Borisenko N.G., Akimova I.V., Gromov A.I., Khalenkov A.M., Merkuliev Yu.A., Kondrashov V.N., Limpouch J., et al. *Fusion Sci. Technol.*, **49** (4), 676 (2006).
14. Benocci R., Batani D., Dezulian R., Redaelli R., Lucchini G., Canova F., Stabile H., et al. *Phys. Plasmas*, **16** (1), 012703 (2009).

15. Hall T., Batani D., Nazarov W., Koenig M., Benuzzi A. *Laser Part. Beams*, **20** (2), 303 (2002).
16. Benuzzi A., Koenig M., Krishnan J., Faral B., Nazarov W., Temporal M., Batani D., et al. *Phys. Plasmas*, **5** (8), 2827 (1998).
17. Canaud B., Fortin X., Garaude F., Meyer C., Philippe F., Temporal M., Atzeni S., Schiavi A. *Nuclear Fusion*, **44** (10), 1118 (2004).
18. Fournier K.B., Satcher J.H., May M.J., Poco J.F., Sorce C.M., Colvin J.D., Hansen S.B., et al. *Phys. Plasmas*, **16** (5), 052703 (2009).
19. Chaurasia S., Leshma P., Murali C.G., Borisenko N.G., Munda D.S., Orekhov A., Gromov A.I., Merkuliev Yu.A., Dhareshwar L.J. *Opt. Commun*., **343**, 1 (2015).
20. Remington B.A., Kane J., Drake R.P., Glendinning S.G., Estabrook K., London R., Castor J., et al. *Phys. Plasmas*, **4** (5), 1994 (1997).
21. Remington B.A., Drake R.P., Takabe H., Arnett D. *Phys. Plasmas*, **7** (5), 1641 (2000).
22. Klein R.I., Budil K.S., Perry T.S., Bach D.R. *Astrophys. J. Suppl. Ser*., **127** (2), 379 (2000).
23. Dong Y., Zhang Lu, Yang J., Shang W. *Phys. Plasmas*, **20** (12), 123102 (2013).
24. Chaurasia S., Kaur C., Rastogi V., Poswal A.K., Munda D.S., Bhatia R.K., Nataraju V. *J. Instrum*., **11** (8), P08004 (2016).
25. Borisenko N.G., Khalenkov A.M., Kmetik V., Limpouch J., Merkuliev Yu.A., Pimenov V.G. *Fusion Sci. Technol*., **51**, 655 (2007).
26. Pimenov V.G., Sheveleva E.E., Sakharov A.M. *Instrum. Exp. Tech*., **59** (2), 321 (2016) [*Prib. Tekh. Eksp*., (2), 156 (2016)].
27. Bugrov A.E., Burdonskii I.N., Gavrilov V.V., et al. *Zh. Eksp. Teor. Fiz*., **111** (3), 903 (1997).
28. Xu Y., Zhu T., Li S., Yang J. *Phys. Plasmas*, **18** (5), 053301 (2011).
29. Wolowski J., Badziak J., Boody F.P., Hora H., Hnatowicz V., Jungwirth K., Krása J., Láska L., Parys P., Pecina V. *Plasma Phys.Controlled Fusion*, **44** (7), 1277 (2002).